Title: Inhibitory interneurons show early dysfunction in a SOD1 mouse model of ALS

Abbreviated Title: Dysfunction of inhibitory interneurons in ALS

C. F. CAVARSAN[1,2], P. R. STEELE[1,2,3], L. M. McCANE[3], K. J. LaPRE[1,2], A. C. PURITZ[4], N. KATENKA[5], AND K. A. QUINLAN[1,2,4]

1 George and Anne Ryan Institute for Neuroscience, University of Rhode Island, Kingston, RI, 02881 USA
2 Department of Biomedical and Pharmaceutical Sciences, College of Pharmacy, University of Rhode Island, Kingston, RI, 02881 USA
3 Interdisciplinary Neuroscience Program, University of Rhode Island, Kingston, RI, 02881 USA
4 Department of Physiology, Northwestern University Feinberg School of Medicine, Chicago, IL, 60611 USA
5 Department of Computer Science and Statistics, University of Rhode Island, Kingston, RI, 02881 USA

Corresponding Author:
Katharina A. Quinlan
kaquinlan@uri.edu
George and Anne Ryan Institute for Neuroscience
University of Rhode Island
130 Flagg Rd
Kingston RI 02881

Number of pages: 30
Number of figures: 5
Number of tables: 4
Number of words in abstract: 150
Number of words in introduction: 619
Number of words in discussion: 1545

Abstract: Few studies in amyotrophic lateral sclerosis (ALS) focus on the premotor interneurons synapsing onto motoneurons (MNs). We hypothesized inhibitory interneurons contribute to dysfunction, particularly if altered before MN neuropathology. We directly assessed excitability and morphology of ventral lumbar glycinergic interneurons from SOD1^{G93A}GlyT2eGFP (SOD1) and wildtype GlyT2eGFP (WT) mice. SOD1 interneurons were smaller but density was unchanged. Patch clamp revealed dampened excitability in SOD1 interneurons, including depolarized PICs and voltage threshold. Renshaw cells (RCs; confirmed with immunohistochemistry) showed similar dampened excitability. Morphology and electrophysiology were used to create a “random forest” statistical model to predict RCs when histological verification was not possible. Predicted SOD1 RCs were less excitable (consistent with experimental results); predicted SOD1 non-RCs were *more* excitable. In summary, inhibitory interneurons show very early perturbations poised to impact MNs, modify motor output, and provide early biomarkers of ALS. Therapeutics like riluzole that universally reduce CNS excitability could exacerbate this dysfunction.

Key words: inhibition, glycine, Renshaw cells, ALS, spinal cord, patch clamp, random forest

Introduction

Amyotrophic lateral sclerosis (ALS) is a rapidly evolving adult-onset neurological disease characterized by a progressive loss of corticospinal neurons and motoneurons (MNs). There has been considerable debate in the field over the role of hyperexcitability in neurodegenerative processes in ALS. While drug treatment for ALS based on nonspecific reduction of neuronal excitability (with riluzole, for example) (Bellingham 2011), does result in a modest increase in lifespan (Bensimon et al., 1994), similar treatment paradigms have been disappointing clinically. A more nuanced understanding of the excitability of vulnerable neurons could help in creating a more targeted and effective approach for treatment of ALS. For example, if inhibitory pathways are failing in ALS and neuronal excitability is universally reduced with riluzole, this could further exacerbate inhibitory dysfunction by reducing activity not only in vulnerable MNs but also in inhibitory interneurons presynaptic to MNs. Thus it is important to consider all aspects of neuronal excitability, including intrinsic excitability of vulnerable neurons, synaptic drive, and neuromodulation (Gunes et al., 2020). Intrinsic properties of MNs have been well studied but the same is not true for interneurons that are synaptically connected to them. In fact, no studies thus far have directly assessed activity of spinal premotor interneurons in an ALS model. Despite evidence that ALS patients have disrupted inhibition at spinal levels (Raynor and Shefner, 1994; Shefner and Logigian, 1998; Sangari et al., 2016; Howells et al., 2020), much is still unknown concerning the involvement of inhibitory circuitry in ALS. Morphological alterations in inhibitory circuits have been demonstrated in animal models of ALS. These include degeneration of spinal interneurons, fewer neurons expressing markers of inhibitory neurotransmitters including GlyT2 prior to loss of MNs (Martin et al., 2007; Hossaini et al., 2011), and loss of glycinergic boutons onto MNs prior to symptom onset (Chang and Martin, 2009a). Typically, fast motor neurons have greater numbers of inhibitory synaptic contacts, but these are largely lost in SOD1 mice beginning when motor unit atrophy is first observed (Pun et al., 2006; Hegedus et al., 2007; Allodi et al., 2020). Recurrent inhibitory circuits mediated by Renshaw cells (RCs) are impaired before symptom onset by both loss of MN collaterals which provide synaptic drive, and complex changes to RC-MN synaptic structures (Casas et al., 2013; Wootz et al., 2013). A few studies have suggested activity is decreased in inhibitory interneurons by indirect measurements. Quantification of synaptic inputs to MNs has shown that frequency of inhibitory postsynaptic potentials in spinal MNs is decreased embryonically in both SOD1 mouse and zebrafish models (McGown et al., 2013; Branchereau et al., 2019) and glycinergic inputs to MNs decay faster in SOD1 MNs (Medelin et al., 2016). On a larger scale, blocking the activity of V1 inhibitory interneurons during *in vivo* treadmill running was recently found to mimic the early locomotor deficits in SOD1 mice

(Allodi et al., 2020), suggesting that inhibitory interneurons could be inactive or under-active. However, none of these studies directly examined electrophysiological activity in inhibitory interneurons.

We hypothesized that inhibitory spinal interneurons could contribute to the pathogenesis of ALS through a depression of MN inhibition. Decreased activity of inhibitory interneurons could result in synaptically-driven hyperexcitability of MNs, and other long-term changes in network function. In this study, we examined electrical and morphological properties of glycinergic interneurons in the spinal cord of SOD^{G93A} GlyT2-eGFP (SOD1) mice compared to GlyT2-eGFP (WT) using whole cell patch clamp and three-dimensional reconstructions, immunohistochemistry for the RC marker calbindin (CBD), and statistical modeling. We show here that significant dysfunction is present in SOD1 glycinergic interneurons, including RCs and other subclasses of inhibitory interneurons. Impairment in glycinergic interneurons should be explored as both a mechanism of vulnerability of MNs and a potential biomarker of early dysfunction of spinal circuits.

Results

Morphology of glycinergic interneurons

Ventrally located glycinergic interneurons in the lumbar enlargement of WT and SOD1 mice postnatal day (P)6-10 were reconstructed from image stacks. There was no change in soma size and density of ventral glycinergic interneurons between WT and SOD1 mice when interneurons throughout the ventral horn were assessed. However, when we narrowed our examination to only those glycinergic interneurons located adjacent to MNs within lamina IX (most likely premotor interneurons), SOD1 interneuron somata were smaller in several measures. Typical ventrolateral glycinergic neurons in the region of the MN pools in lamina IX are shown in the areas delimited with dotted lines in **Figure 1A**. Complete reconstructions of soma morphology were performed on 3902 GlyT2 interneurons (1918 WT and 1984 SOD1 interneurons) from fixed lumbar spinal cords (image stacks obtained using confocal microscopy) and 682 GlyT2 interneurons from only lamina IX (362 WT and 320 SOD1 interneurons). Reconstructions revealed that glycinergic interneurons in lamina IX were significantly smaller in every measurement of the soma (soma perimeter, largest cross-sectional area, soma surface area, and soma volume) (Fig 1B). Cell counts performed in the ventral lumbar spinal cord of 8 WT mice and 9 SOD1 mice showed no significant differences (Fig 1C). Dendritic morphology was not possible in these images due to the high number of GFP+ neurons and processes but was completed on a smaller subset of neurons that were imaged live after patch clamp electrophysiology with a 2-photon microscope.

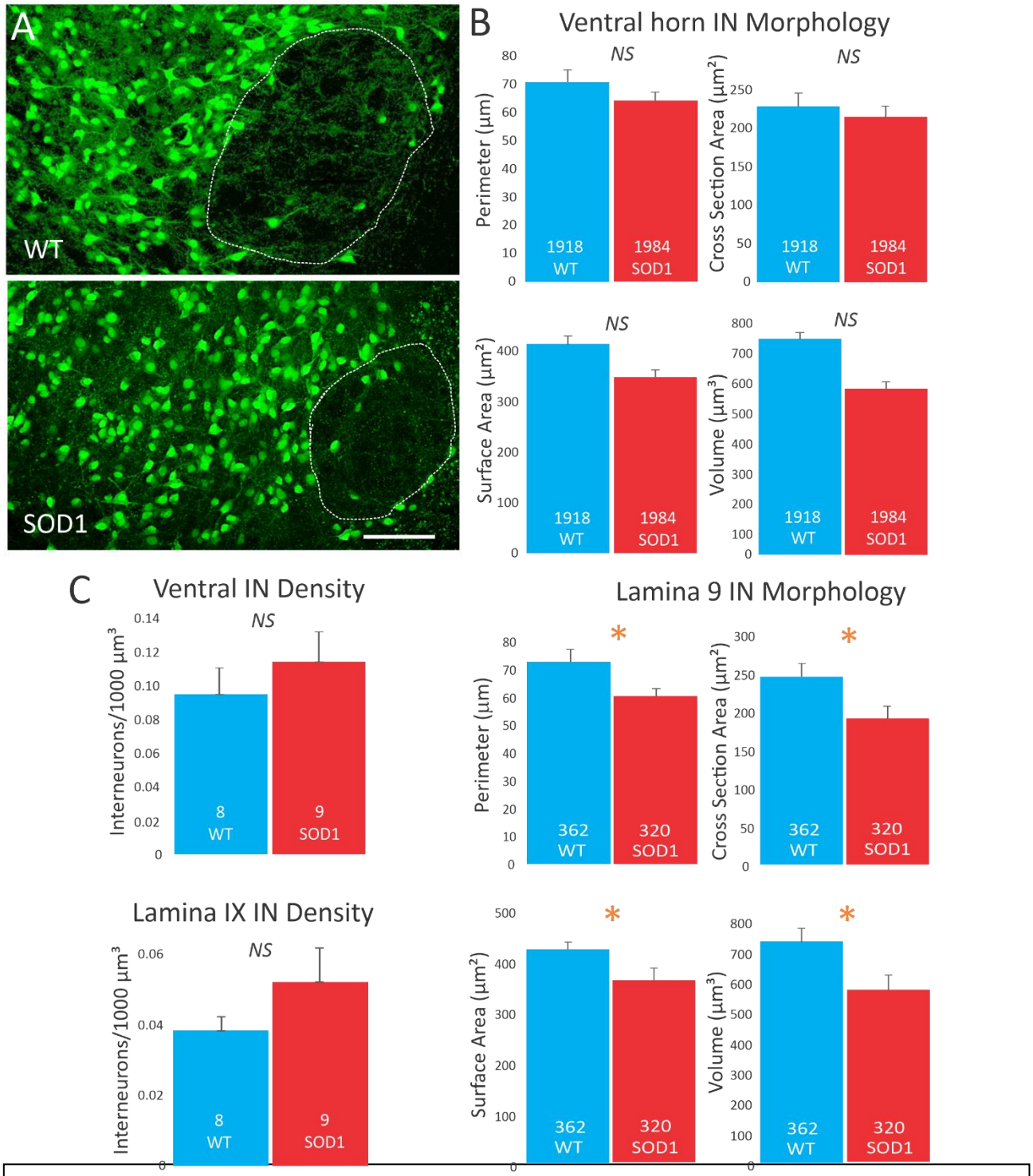

Figure 1: GlyT2 interneurons in the ventral horn and lamina IX from WT and SOD1 mice were counted and morphologically analyzed. Representative images of GFP interneurons in **A**, WT on the top and SOD1 on the bottom. Lamina IX delimited with dotted lines in images of ventral horns. (**B**) Morphological analysis showed no differences between glycinergic neurons in the ventral horn (top panels), but within lamina IX (bottom panels), SOD1 GlyT2 interneurons were smaller than WT in soma perimeter, soma largest cross-sectional area, soma surface and soma volume. (**C**) Density of GlyT2 interneurons were not significantly different between WT and SOD in the ventral horn or in lamina IX. Significance denoted with * indicates $p \leq 0.05$. Scale bar in A: 100 µm.

In these experiments, 59 glycinergic neurons (34 WT and 25 SOD1) were recorded using visually guided patch clamp with Texas Red dye in the electrode as shown in **Figure 2A.** The location of patched neurons was distributed throughout the ventral horn, not limited to lamina IX (Fig 2B). Thus, similar to the larger dataset above, soma sizes of patched SOD1 interneurons were not significantly smaller than WT (Fig 2C). However, dendrites were larger in patched SOD1 GlyT2 interneurons, including greater dendritic surface area and volume (see **Table 1** for complete results).

Electrophysiology of glycinergic interneurons

Whole cell patch clamp revealed very different intrinsic properties of ventral glycinergic interneurons. Recording was performed on 59 ventral interneurons from throughout the ventral horn (not limited to lamina IX) in transverse lumbar spinal cord slices from P6-10 mice. SOD1 inhibitory interneurons (n = 25) were found to have diminished intrinsic excitability compared to WT interneurons (n = 34). Measurements of intrinsic excitability included depolarized onset and peak voltage of persistent inward currents (PICs) and depolarized threshold for action potential firing, as shown in **Figure 3**. In voltage clamp, slowly depolarizing voltage ramps were used to measure PICs (typical leak subtracted traces shown in Fig3A). Voltage sensitivity is determined by measuring voltage at PIC onset and peak. Both PIC onset and peak were significantly depolarized in SOD1 interneurons, indicating less intrinsic excitability. Amplitude of the PIC was unchanged. Depolarizing current ramps were used to measure the input-output relationship of the neurons in current clamp. Inhibitory interneurons from SOD1 mice were found to have significantly higher threshold voltage than control interneurons (Fig 3E-F). This shift is likely driven by the changes in PIC. The current at firing onset, or I-ON, was not significantly changed (p = 0.15), similar to the current at firing offset, or I-OFF (p = 0.07). After-spike afterhyperpolarization (AHP) was also significantly different in SOD1 interneurons. The duration (at half AHP amplitude) was shorter in SOD1 neurons, as shown in Fig 3H-I. Amplitude of the AHP was unchanged. While changes in the PIC and threshold indicate less excitability in SOD1 interneurons, the shortened AHP suggests an increased ability to fire at higher rates in SOD1 interneurons, a property that is associated with increased excitability. However, no changes in firing rates were detected in SOD1 interneurons. All other properties were found to be similar in SOD1 and WT glycinergic interneurons, including maximum firing rates, sag/rebound currents (I_H), action potential parameters and membrane properties (see **Table 2** for all electrical properties). See discussion for further interpretation of these findings.

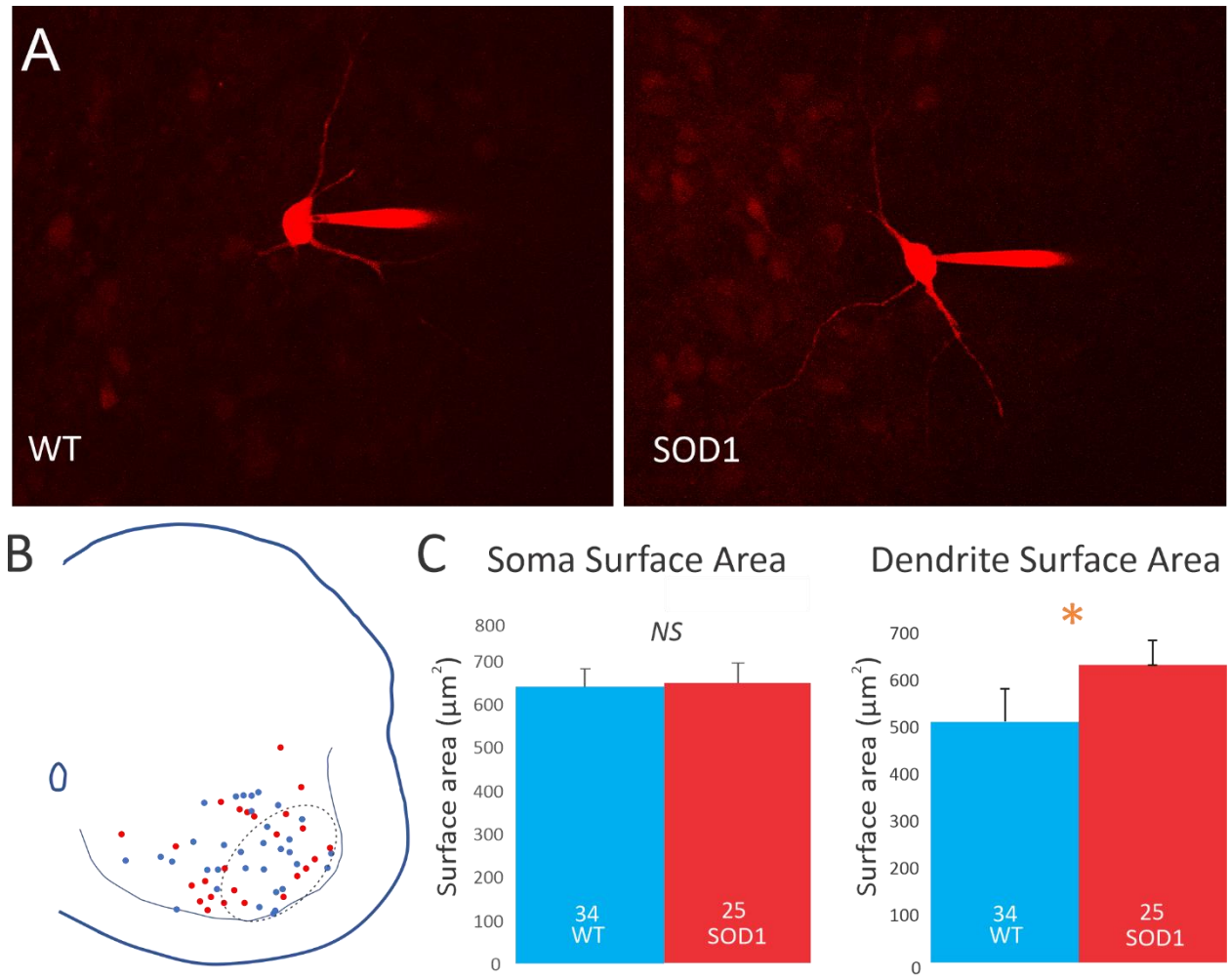

Figure 2 GlyT2 interneurons from WT and SOD1 mice were patched throughout the ventral horn. Images of typical interneurons in **A**, and locations of all patched interneurons in **B** (WT = blue, SOD1 = red), with dotted line indicating area of lamina IX. **(C)** In patched interneurons, soma surface area was unchanged, while dendrite surface area was larger in SOD1 interneurons than in WT. Significance denoted with * indicates $p \leq 0.05$.

134
135

136 **Table 1:** Reconstruction data of GlyT2-GFP+ interneurons in WT and SOD1 animals.

		WT (Mean ± SE)	SOD (Mean ± SE)	*p*
GlyT2-GFP+ Interneurons				
Ventral horn		N = 1918	N = 1984	
Soma	Perimeter (µm)	70.8 (± 4.4)	64.3 (± 2.5)	0.200
	Cross Sectional Area (µm²)	229.2 (± 17.3)	215.1 (± 14.4)	0.535
	Surface Area (µm²)	413.4 (± 21.7)	348.9 (± 22.8)	0.115 [K]
	Volume (µm³)	714.0 (± 64.3)	552.1 (± 54.6)	0.115 [K]
Lamina IX		N = 362	N = 320	
Soma	Perimeter (µm)	70.0 (± 4.4)	58.1 (± 2.5) *	0.034 [K]
	Cross Sectional Area (µm²)	240.2 (± 17.0)	186.9 (± 15.9) *	0.031
	Surface Area (µm²)	421.7 (± 13.9)	358.2 (± 21.9) *	0.025
	Volume (µm³)	731.7 (± 44.1)	568.4 (± 49.5) *	0.022
Patched GlyT2-GFP+ Interneurons				
		N = 34	N =25	
Soma	Perimeter (µm)	68.4 (± 3.4)	61.6 (± 3.0)	0.082
	Cross Sectional Area (µm²)	174.4 (± 13.4)	183.1 (± 16.9)	0.813[K]
	Surface Area (µm²)	637.5 (± 40.3)	644.3 (± 47.6)	0.903[K]
	Volume (µm³)	1472.4 (± 165.8)	1611.1 (± 188.9)	0.523[K]
Dendrites	Length (µm)	101.4 (± 17.3)	106.3 (± 10.0)	0.116[K]
	Surface Area (µm²)	512.7 (± 70.6)	633.6 (± 52.1) *	0.024[K]
	Volume (µm³)	264.7 (± 39.6)	375.3 (± 37.9) *	0.010[K]

137 Significance denoted with * indicates $p \leq 0.05$.

138 [K] Indicates Kruskall Wallis analysis for non-normal distributions; all others were ANOVA analysis.

139

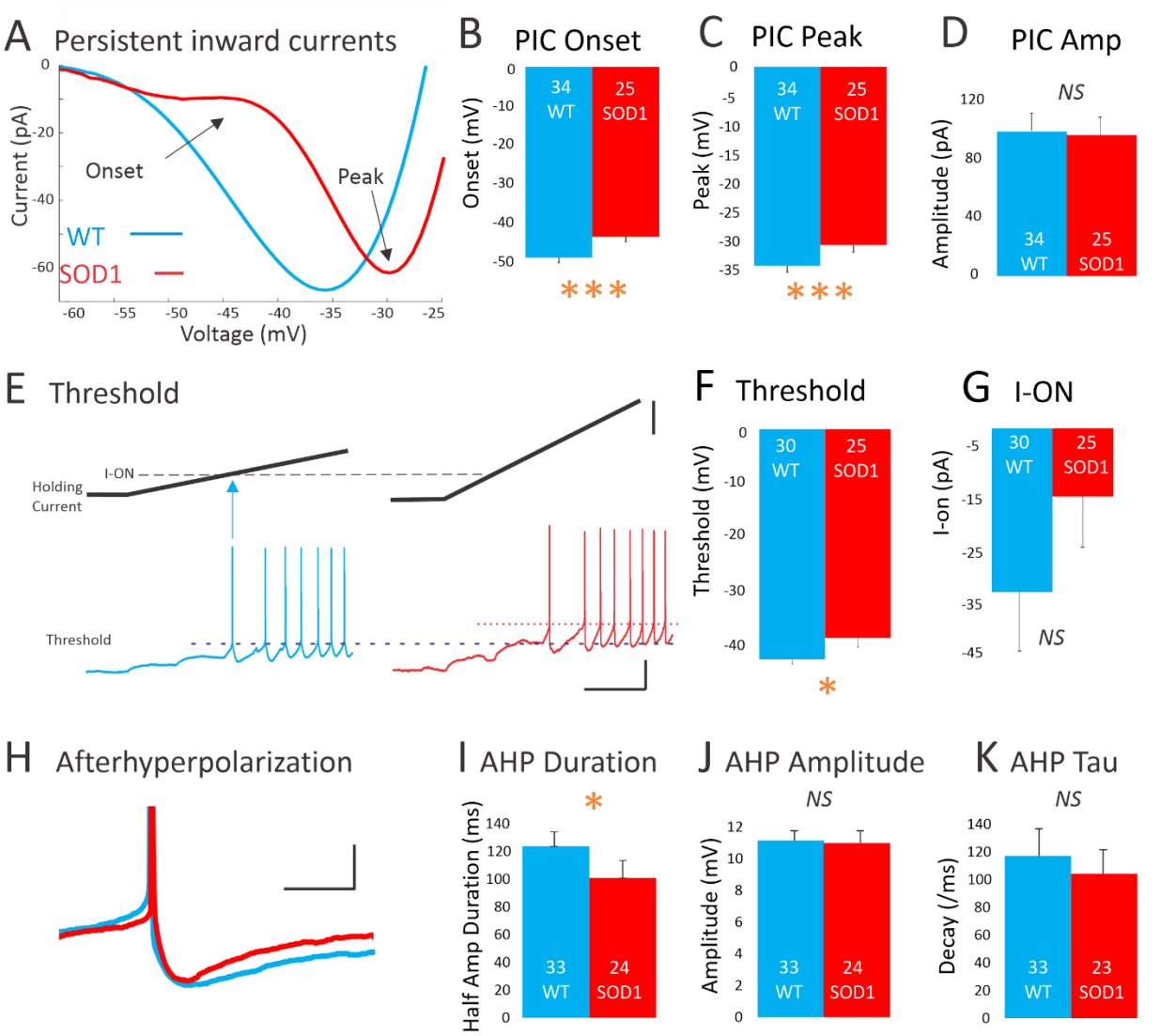

140

Figure 3: Electrophysiology of SOD1 glycinergic interneurons. The most prominent difference in SOD1 interneurons was the shift in voltage dependence of PICs. (**A**) Representative, leak-subtracted current-voltage relationship of PICs from WT (P8) and SOD1 (P6) interneurons; arrows indicate voltage at PIC onset and voltage at PIC peak. (**B-D**) Mean onset, peak and amplitude of PICs in WT and SOD1 interneurons. (**E-F**) Threshold voltage (as measured by current ramps as shown) was depolarized in SOD1 interneurons. Starting potential for both interneurons was -65mV. The current at firing onset (I-ON) was not significantly different as shown in **G.** (**H**) The AHP in SOD1 interneurons was shorter, as shown by the smaller mean duration at half amplitude in a representative P8 WT and P7 SOD1 interneuron in **I.** Neither the AHP amplitude nor the AHP decay time constant, tau, were significantly altered in SOD1 glycinergic interneurons as shown in **J-K.** Vertical scale bars in E: top = 50pA, and bottom = 20mV. Horizontal scale bar in E = 0.5s and all scale bars apply to both left and right panels. Vertical scale bar in H = 10mV (APs were truncated from image), and horizontal scale bar = 50ms. Significance denoted with * indicates $p \leq 0.05$.

141

142

143 **Table 2:** Electrophysiological properties of GlyT2-GFP+ interneurons in WT and SOD1 animals.

Parameters	Groups		
	WT (Mean ± SE)	SOD (Mean ± SE)	*p*
	N = 34	*N* = 25	
Resting membrane potential (mV)	-46.7 ± 1.1	-45.7 ± 1.4	0.524[K]
Capacitance (pF)	66 ± 7	55 ± 5	0.529[K]
Input resistance (MΩ)	295 ± 32	299 ± 41	0.794[K]
PIC properties			
PIC onset (mV)	-50.5 ± 1.0	-46.3 ± 1.0*	0.004
PIC peak (mV)	-35.1 ± 0.8	-31.2 ± 0.9*	0.003
PIC amplitude (pA)	100 ± 13	97 ± 12	0.890[K]
Normalized PIC (pA/pF)	1.79 ± 0.24	1.92 ± 0.22	0.226[K]
Firing properties			
Inst max firing freq range max (Hz)	112 ± 8	113 ± 8	0.961
Inst max firing freq range min (Hz)	55 ± 3	63 ± 7	0.442[K]
Steady state firing freq range max (Hz)	36 ± 2	40 ± 3	0.355[K]
Steady state firing freq range min (Hz)	6 ± 0.4	6 ± 0.7	0.453[K]
I-ON (pA)	-33 ± 12	-14 ± 11	0.148[K]
I-OFF (pA)	5 ± 9	36 ± 14	0.074[K]
Δ I (pA)	38 ± 8	50 ± 10	0.331[K]
AP properties			
AP overshoot past 0 (mV)	20.0 ± 1.7	21.4 ± 1.6	0.553
AP duration at half peak (ms)	1.53 ± 0.10	1.48 ± 0.08	0.944
AP rate of rise (V/s)	87 ± 5	83 ± 3	0.428[K]
AP rate of fall (V/s)	45 ± 3	43 ± 2	0.924[K]
Threshold on ramp (mV)	-40.6 ± 0.8	-37.9 ± 1.1*	0.052[K]
Threshold on step (mV)	-47.3 ± 0.8	-45.1 ± 1.3	0.199[K]
AHP properties			
AHP amplitude (mV)	11.2 ± 0.6	11.0 ± 0.8	0.704[K]
AHP duration at half amplitude (s)	0.12 ± 0.01	0.10 ± 0.01*	0.045[K]
AHP tau (s^{-1})	0.12 ± 0.02	0.10 ± 0.02	0.980[K]
I_H properties			
Hyperpolarizing Sag (%)	32 ± 3	32 ± 4	0.537[K]
Depolarizing Rebound (%)	17 ± 3	19 ± 5	0.536[K]

144 Significance denoted with * indicates $p \leq 0.05$.

145 [K] Indicates Kruskall Wallis analysis for non-normal distributions; all others were ANOVA analysis.

146

147 **Renshaw cells: electrophysiology and morphology**

148 Glycinergic interneurons in the ventral spinal cord are not a homogenous population and we sought to
149 determine more specifically what subtype of ventral inhibitory interneurons were morphologically and
150 electrophysiologically altered in SOD1 mice. Since we recorded glycinergic interneurons in the region of
151 lamina IX, we expected our population to include RCs. To distinguish them, we performed
152 immunohistochemistry for the RC marker CBD on GlyT2 neurons labeled with dye during recording (see
153 **Figure 4A**). We also examined density of RCs in lamina IX of the spinal cords, which was unchanged
154 between WT (N = 8 mice) and SOD1 (N = 7 mice; Figure 4B). Similar to the results above for all GlyT2
155 interneurons, electrophysiological parameters of SOD1 RCs were very different compared to WT (7 WT
156 and 6 SOD interneurons). The voltage dependence of the PIC (both onset and peak) was significantly
157 depolarized in SOD1 RCs, indicating they are less excitable. Threshold voltage was also significantly
158 higher in SOD1 RCs when measured from step protocols, though it was not significant when measured
159 from current ramp protocols (Figure 4C). All RC electrophysiological properties are included in **Table 3**.
160

161

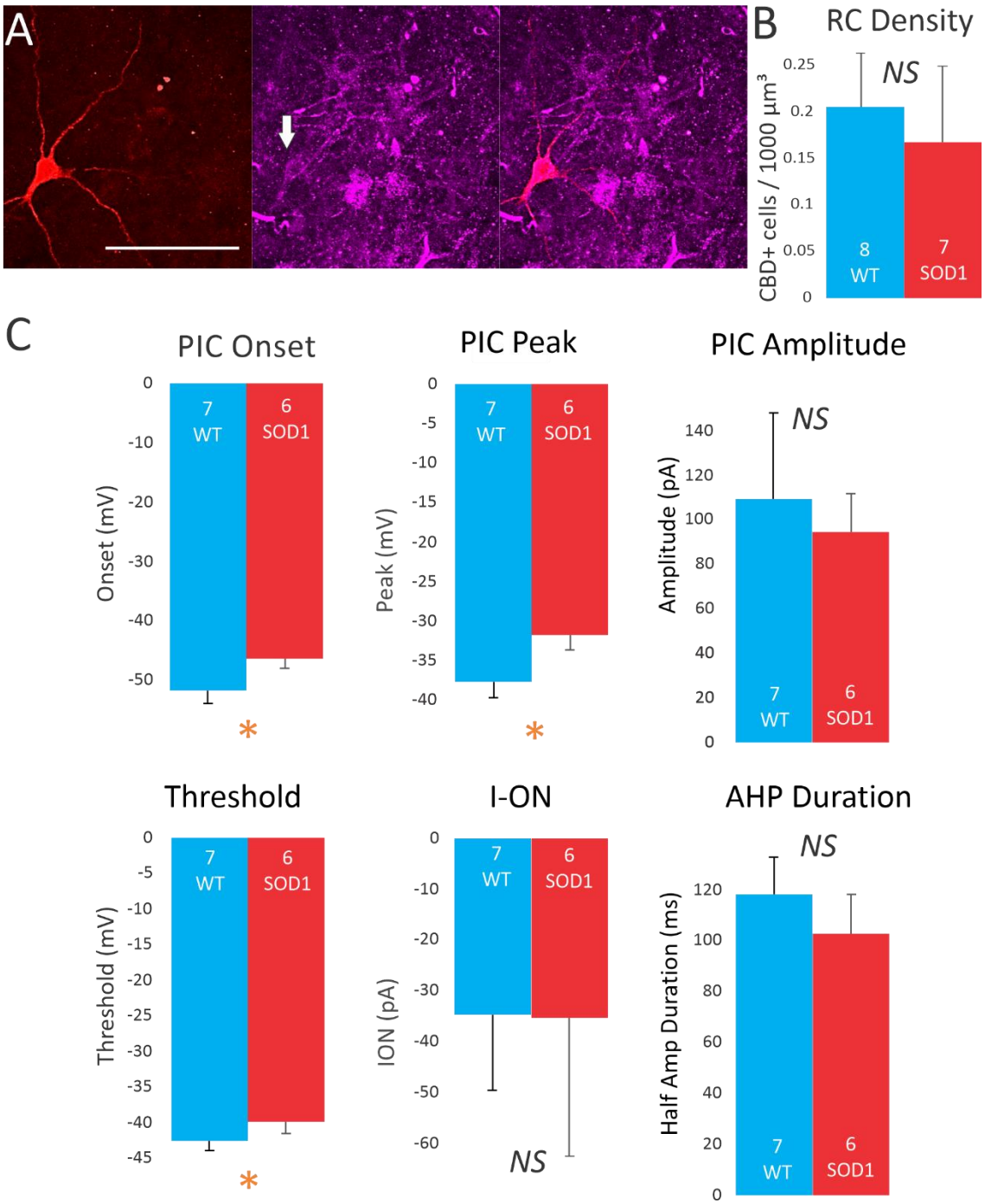

Figure 4: Renshaw cell (RC) density and electrophysiology. (**A**) Image of an interneuron which was patched and filled with Texas Red (left panel), and immunoreactive for CBD (middle panel); overlay provided in right panel. The RC is indicated by a white arrow in middle panel. (**B**) No differences were found in the density of CBD+ cells in lamina IX of WT and SOD1 mice. (**C**) Several electrophysiological parameters were measured from the cells. PIC onset, PIC peak and voltage threshold showed higher values in RCs from SOD1 animals, compared to WT RCs. There were no significant differences between groups in PIC amplitude, I-on and AHP duration. Significance denoted with * indicates $p \leq 0.05$. Scale bar in A: 100 µm.

163 **Table 3:** Electrophysiological properties of Renshaw cells, in both groups, WT and SOD1.

Parameters	Groups		
	WT (Mean ± SE)	SOD (Mean ± SE)	*p*
	N = 7	N = 6	
PIC properties			
PIC onset (mV)	-53.7 ± 2.5	-46.3 ± 1.9*	0.040
PIC peak (mV)	-39.4 ± 2.2	-31.8 ± 2.0*	0.027
PIC amplitude (pA)	109.4 ± 41.6	94.6 ± 18.7	0.775 [K]
Normalized PIC (pA/pF)	1.76 ± 0.41	2.13 ± 0.47	0.475 [K]
Firing properties			
Inst max firing freq range max (Hz)	120.8 ± 24.9	122.3 ± 17.4	0.962
Inst max firing freq range min (Hz)	55.8 ± 9.2	62.0 ± 7.1	0.608
Steady state firing freq range max (Hz)	43.0 ± 8.1	43.7 ± 7.6	0.954
Steady state firing freq range min (Hz)	4.8 ± 0.5	7.8 ± 1.7	0.097
I-ON (pA)	-34.8 ± 15.9	-35.1 ± 29.7	0.985
I-OFF (pA)	7.9 ± 20.8	12.6 ± 37.7	0.475 [K]
Δ I (pA)	42.7 ± 14.9	48.0 ± 16.1	0.567 [K]
AP properties			
AP overshoot past 0 (mV)	21.3 ± 4.0	23.9 ± 4.1	0.661
AP duration at half peak (ms)	1.2 ± 0.1	1.4 ± 0.1	0.452
AP rate of rise (V/s)	99.1 ± 5.7	94.1 ± 4.0	0.501
AP rate of fall (V/s)	54.2 ± 5.7	47.5 ± 3.6	0.359
Threshold on ramp (mV)	-42.6 ± 1.4	-39.8 ± 1.9	0.262
Threshold on step (mV)	-48.7 ± 1.1	-45.0 ± 1.0*	0.032
AHP properties			
AHP amplitude (mV)	12.6 ± 1.1	11.2 ± 1.7	0.481
AHP duration at half amplitude (s)	0.118 ± 0.016	0.103 ± 0.017	0.516
AHP tau (s^{-1})	0.103 ± 0.022	0.082 ± 0.014	1.000 [K]
I_H properties			
Hyperpolarizing Sag (%)	35.3 ± 6.7	44.8 ± 11.5	0.471
Depolarizing Rebound (%)	19.1 ± 4.1	30.1 ± 17.4	0.568 [K]

164

165 Significance denoted with * indicates $p \leq 0.05$.

166 [K] Indicates Kruskall Wallis analysis for non-normal distributions; all others were ANOVA analysis.

167

Predictive statistical modeling

Since it was not possible to identify all recorded GlyT2 neurons as RCs or non-RCs using immunohistochemistry, we performed predictive statistical modeling. We created a series of statistical models using random forest and principal components analysis (see methods for more details on creation of the models). All variables, including morphology and electrical properties, were grouped into 8 categories of related variables. For example, all variables pertaining to dendritic morphology were grouped into a single category. Importance of each variable was determined by the decrease in accuracy of the model when variables were removed. The variables that were used by the random forest model are listed in **Table 4** in descending order of importance. Variables with large positive values were crucial for the model's accuracy in predicting RC vs non-RCs, while variables that have negative values proved detrimental to the predictive value of the model. For comparison, the grouping that provided the best prediction of CBD-tested neurons using PCA were action potential features (LOOCV accuracy 70%, AIC =28, p=0.11 and 0.08, PC1 and PC2, respectively). Variables in this grouping that had effect sizes ≥ 0.5 were I-off, AP threshold, AP rise and AP fall. The most accurate random forest model correctly predicted the identity of the CBD-tested interneurons with 79% accuracy; thus we used this model to predict RCs and non-RCs in all recorded GlyT2+ interneurons in which RC identification using immunohistochemistry was not possible. The model predicted that 80% of our 59 patched interneurons were RCs. This percentage is greater than that measured from our immunohistochemistry results: 65% of our patched interneurons (15/23) were positive for CBD. Predicted RCs were then analyzed as a group for differences between WT and SOD interneurons, while predicted non-RCs were analyzed separately. We found that in predicted RCs, there was a depression of excitability very consistent with our experimental data. The predicted RC grouping had significant depolarization of the PIC and significantly depolarized threshold. PIC parameters of the predicted groups are shown in **Figure 5**. Interestingly, in predicted non-RCs excitability increased. Both the PIC amplitude and the PIC normalized to capacitance were larger in the group of predicted non-RCs from SOD1 mice. Further studies will be needed to investigate more fully the properties of different subtypes of non-RC glycinergic interneurons in this and other ALS models at this and other time points in the lead up to MN dysfunction and degeneration.

196

197 **Table 4:** Variables used to create the random forest predictive model. Variables are arranged in
198 descending order of importance for prediction of RCs and non-RCs, based on the mean decrease in
199 accuracy test.
200

Variable	Mean Decrease in Accuracy
Dendrite Mean Length (µm)	8.27508593
Cell Body Surface Area (µm^2)	3.98158541
Capacitance (pF)	3.82644995
AHP tau (s^{-1})	3.42103087
Cell Body Length (µm)	2.97501036
Perimeter (µm)	2.15259564
Dendrite Surface Area (µm^2)	1.58220831
Cell Body Volume (µm^3)	1.30757721
Cell Body Surface Area (µm^2)	1.17777719
V threshold (mV)	0.99130144
Cell Body Area (µm^2)	0.89067177
AP size (mV)	0.59738713
Enclosed Volume (µm^3)	0.57054623
Steady state firing freq max (Hz)	0.28434868
I-ON (pA)	0.13715380
I_H Sag (mV)	-0.06241806
Dendrite Volume (µm^3)	-0.41041638
Dendrite Length (µm)	-0.91989565
Instantaneous max firing rate (Hz)	-0.96322954
Inst max firing freq range max (Hz)	-1.40411698
AP overshoot (mV)	-1.53244473
I_H Rebound (mV)	-1.95402459

201

202

203

204

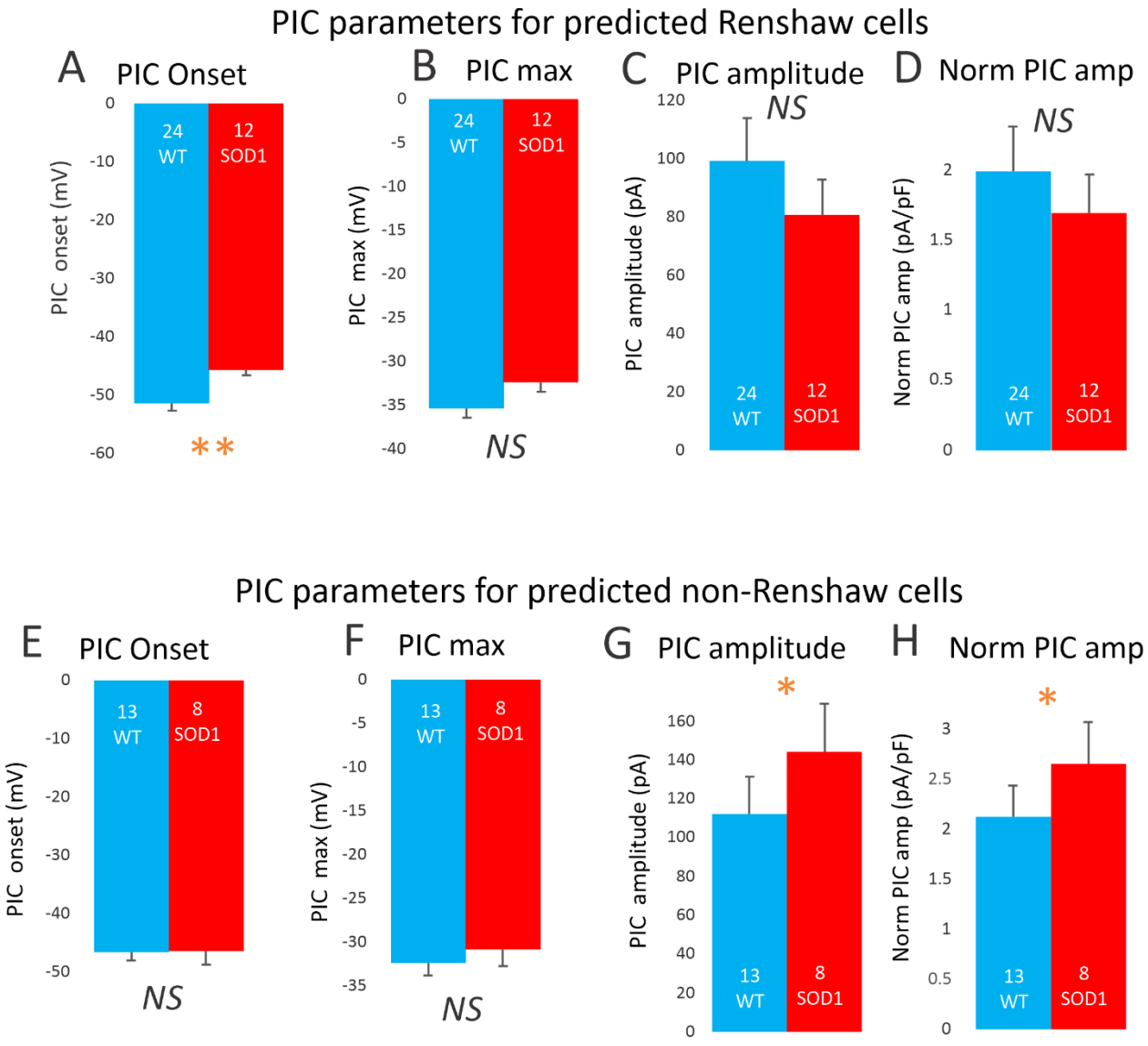

Figure 5 Genotype is predicted to have opposite effects on predicted RCs and non-RCs. **A – D** Predicted RCs have depolarized PIC onset, similar to overall experimental results. This is accompanied by depolarized threshold (data not shown). **E – H** Predicted non-RC glycinergic interneurons have larger PIC amplitudes, including larger normalized PIC amplitudes. * Significance denoted with * indicates $p \leq 0.05$.

205

206

207

Discussion

This study shows for the first time that RC are depressed in excitability and glycinergic interneurons may be contributing to ALS pathology. Alterations in both morphology and excitability of glycinergic interneurons occurs at a very early stage. RCs are depressed in activity and lamina IX interneurons are smaller in SOD1 mice. Based on our statistical modeling, we predict the remaining non-RC inhibitory interneurons have increased excitability, including larger PICs. We speculate that these shifts in interneuron excitability could alter the excitability of postsynaptic MNs, modify motor output, and provide an early biomarker of ALS.

Intrinsic and synaptic hyperexcitability

A core issue this study brings to light is potential long-term disruption to the balance of excitatory and inhibitory synaptic transmission in ALS. Spinal cord and cortex both show imbalance between excitatory and inhibitory synaptic transmission in SOD^{G93A} mice (Avossa et al., 2006; Saba et al., 2016). Clinically, ALS patients show evidence of altered synaptic activity as well, including a reduction in inhibition. A reduction of glycinergic receptor binding in the anterior gray matter of the spinal cord (Hayashi et al., 1981; Whitehouse et al., 1983) has been demonstrated along with abnormal glycine and gamma amino butyric acid (GABA) levels in blood serum (Malessa et al., 1991; Niebroj-Dobosz and Janik, 1999). Electrophysiology also suggests disruption in spinal inhibitory circuits in ALS patients (Raynor and Shefner, 1994; Shefner and Logigian, 1998; Sangari et al., 2016). An interesting question is whether the neurons are altered in excitability only within the motor circuit (i.e. corticospinal neurons and the synaptically-connected spinal inhibitory and cholinergic interneurons, and MNs), or if disturbances are more widespread throughout the nervous system. In the spinal cord, interneurons that serve as conduits between vulnerable corticospinal and spinal MNs include cholinergic interneurons, Ia inhibitory interneurons and RCs. There is abundant evidence of disruption in these cholinergic, GABAergic and glycinergic synapses from animal models (Martin et al., 2007; Chang and Martin, 2009b; Pullen and Athanasiou, 2009; Hossaini et al., 2011; Herron and Miles, 2012; Casas et al., 2013; Wootz et al., 2013; Saxena et al., 2013; Milan et al., 2015; Dukkipati et al., 2016; Medelin et al., 2016). Similarly, in the cortex, neurons that are not themselves vulnerable to neurodegeneration in ALS also exhibit altered excitability and morphology in a parallel time course to the vulnerable corticospinal neurons (Clark et al., 2017, 2018; Kim et al., 2017). The changes in excitability of other neuronal populations must contribute to the imbalance of both excitatory and inhibitory neurotransmission that has been clearly demonstrated in ALS patients and animal models.

A case for hyperexcitability and glutamate excitotoxicity involvement in ALS pathogenesis has been more controversial. Altered intrinsic excitability has been consistently reported in both corticospinal projection neurons and spinal MNs, but these perturbations appear to fluctuate based on age/disease progression. Corticospinal projection neurons have increased firing and other signs of hyperexcitability during the first week of postnatal development (Pieri et al., 2009; Saba et al., 2016, 2019; Kim et al., 2017), but excitability is normal in young and adult pre-symptomatic ages (Kim et al., 2017; Saba et al., 2019), and may become hypoexcitable at the age of symptom onset (Saba et al., 2019). Similarly, spinal MNs show intrinsic hyperexcitability at very early (embryonic) stages (Kuo et al., 2004, 2005; Martin et al., 2013). At a postnatal age similar to the inhibitory interneurons in this study, spinal MNs do *not* have an altered threshold, rheobase or frequency-current relationship, though other abnormalities are present in PICs, action potential duration, AHP and dendritic Ca^{2+} entry (Pambo-Pambo et al., 2009; Quinlan et al., 2011, 2015; Leroy et al., 2014). Thus, at the time point studied here, inhibitory interneurons are more disrupted in excitability than the vulnerable spinal MNs. At symptom onset, MNs may finally succumb to hypo excitability, though not all studies agree on this point (Delestrée et al., 2014; Martinez-Silva et al., 2018; Jensen et al., 2020). Notably, MNs derived from ALS patients' induced pluripotent stem cells also show initial hyperexcitability followed by hypoexcitability (Wainger et al., 2014; Devlin et al., 2015), and increasing excitability of MNs enhanced neuroprotection rather than neurodegeneration (Saxena et al., 2013). A unifying theme throughout the findings is that vulnerable MNs show excessive homeostatic gain in response to perturbation (Kuo et al., 2020), and not only excitability but other cellular properties wildly fluctuate over the lifespan of the animal (Irvin et al., 2015). In light of that, the present findings that inhibitory interneurons are less excitable should be further explored to fully characterize their contribution to neurodegenerative processes.

Changes in neuron morphology

In ALS models, altered morphology in spinal MNs occurs so early that it could be viewed as a deficit in normal development. Embryonically, SOD1 MNs have shorter projections but this is reversed during postnatal development. At 1-2 weeks of age, MNs begin to show more dendritic branching and larger soma sizes (Amendola and Durand, 2008; Filipchuk and Durand, 2012; Martin et al., 2013). Spinal MNs remain larger through adulthood (Dukkipati et al., 2018). In contrast to the spinal MNs at this age, we found that inhibitory interneurons in lamina IX were smaller and patched interneurons had expanded dendritic surface area and volume. This is reminiscent of changes in corticospinal neurons: presymptomatic corticospinal neurons also have increased arborization but with smaller soma

diameters (Ozdinler et al., 2011; Saba et al., 2016). In both sporadic and familial ALS patients, postmortem tissue shows degeneration of apical dendrites in corticospinal neurons and smaller soma size (Genç et al., 2017). Changes in neuronal size over the life span could greatly increase the impact of other stressors (e.g., proteostasis, metabolic deficits, intracellular transport) on vulnerable neuron populations.

After spike afterhyperpolarization

The AHP can contribute to a neuron's firing rate such that a neuron with a large, long-lasting AHP will typically fire at a slower rate (typical of slow/type I MNs) than a neuron with small, fast-decaying AHP (typical of fast/type II MNs). In ALS patients, AHP is shortened in MNs of patients with little force deficits and later elongated in patients with large force deficits (Piotrkiewicz and Hausmanowa-Petrusewicz, 2011), which could reflect early changes in physiology of vulnerable fast MNs and later, the remaining, less-vulnerable population of slow MNs. Similarly, SOD1 mouse MNs show shorter AHPs early, and longer AHPs around symptom onset (Quinlan et al., 2011; Jensen et al., 2020). Here we show that AHP is shorter in duration in SOD1 interneurons very early, however we did not find changes in any measure of the minimum or maximum firing rates in GlyT2 interneurons or RCs, so the physiological importance of this finding is not clear.

Inhibitory interneurons: Subtype specific effects

The interneurons in this study were mostly composed of RCs, based on both our positivity rate with immunohistochemistry for CBD (65% positive) and our statistical modeling (80% RC / 20% non-RC). Interneurons located in lamina IX likely reflect a mix of RCs and Ia inhibitory interneurons. Based on highly significant results in our RC group and the prediction of higher excitability in non-RC inhibitory interneurons, further studies are warranted to examine how inhibitory interneurons may be differently modulated in a subtype-specific manner in animal models of ALS.

Functional implications for impaired inhibitory circuits

Outward signs of improperly functioning inhibitory interneurons may be apparent from subtle changes in motor patterning and could potentially be used as a biomarker of early ALS. Locomotor disturbances have been demonstrated *in vivo* in presymptomatic SOD1 mice during walking/running (Vinsant et al., 2013a, 2013b; Akay, 2014; Quinlan et al., 2017; Allodi et al., 2020). In the embryonic and neonatal spinal cord *in vitro*, increased duration of depolarizing events in MNs and a slower period of locomotor-related bursting has been described (Medelin et al., 2016; Branchereau et al., 2019), which indicate that even during development the functioning of locomotor circuits is already impaired. In presymptomatic adult

mice capable of running on a treadmill, subtle locomotor differences are observed including advanced intermuscular phasing and a slower speed (Quinlan et al., 2017; Allodi et al., 2020) which indicate that before any large scale neurodegeneration occurs, there are changes in patterns of activity in MNs and interneurons that could be exploited for use as a biomarker of ALS. At initial symptom onset, the first failure of the tibialis anterior manifests as abnormality in the swing phase of the ankle (Akay, 2014). Interestingly, silencing different interneuron populations (including inhibitory interneurons and cholinergic interneurons) reveals the contribution of each population: silencing cholinergic interneurons increases locomotor deficits in SOD1 mice (Landoni et al., 2019), while silencing inhibitory interneurons has no effect suggesting these interneurons are already impaired (Allodi et al., 2020).

Clinical-translational implications

Evidence of MN hyperexcitability in ALS patients is present alongside signs of dysfunction in inhibition (Rothstein et al., 1992; Plaitakis and Constantakakis, 1993; Raynor and Shefner, 1994; Shefner and Logigian, 1998; Andreadou et al., 2008; Bae et al., 2013). Perhaps reducing excitability (with riluzole, for example) only results in a modest increase in lifespan (Bensimon et al., 1994) because it could be helpful to MNs while exacerbating inhibitory dysfunction by further depressing excitability of inhibitory interneurons like RCs. Thus, a more targeted approach to reduce MN excitability could be beneficial early in disease pathology. Stimulation of inhibitory nerves or certain protocols of transcranial stimulation could be explored, along with augmentation of inhibitory neurotransmission.

Materials and Methods

Ethics Statement

Experiments were performed in accordance with the United States National Institutes of Health Guide for Care and Use of Laboratory Animals. Approval of the Northwestern University's Animal Care and Use Committee was obtained for all experiments performed in this study. All efforts were made to minimize animal suffering and to reduce the number of animals used.

Animals and Tissue harvest

Transgenic B6SJL mice overexpressing the human *SOD1*^{G93A} gene (strain 002726, Jackson Labs, Bar Harbor, ME, USA) and their wild type littermates were used (nontransgenic for the human *SOD1*^{G93A} gene). Transgenic animals were identified using standard PCR techniques by Transnetyx (Cordova, TN, USA) and were bred with GlyT2-eGFP mice (Zeilhofer et al., 2005) generating SOD1^{G93A} GlyT2-eGFP mice, here called SOD1. Inhibitory glycinergic interneurons express the Na^+ and Cl^- coupled glycine transporter 2, or GlyT2. GlyT2-eGFP expression is driven by the GlyT2 promotor. Specifically, GlyT2-eGFP females were bred with SOD1^{G93A} GlyT2-eGFP males, and progeny were used for experiments without knowing if they were SOD1^{G93A} GlyT2-eGFP or GlyT2-eGFP. Genotyping was performed post-experimentally. For the following studies juvenile mouse pups were used between postnatal day (P) 6 - 10. Mice were deeply anesthetized with isoflurane (Henry Schein Animal Health, Dublin, OH, USA), decapitated and eviscerated. The lumbar spinal cord from L1 - L6 was removed and embedded in 2.5% w/v agar (No. A-7002, Sigma-Aldrich, St Louis, MO, USA). The agar block was then superglued with Loctite 401 (Henkel Corporation, Rocky Hill, CN, USA) to a stainless steel slicing chuck and 350 µm transverse slices were made using the Leica 1000 vibratome (Leica Microsystems, Buffalo Grove, IL, USA) as described previously (Quinlan et al., 2011). During both spinal cord isolation and slicing, the spinal cord was immersed in 1–4°C high osmolarity dissecting solution containing (mM): sucrose 234.0, KCl 2.5, $CaCl_2 \cdot 2H_2O$ 0.1, $MgSO_4 \cdot 7H_2O$ 4.0, HEPES 15.0, glucose 11.0, and Na_2PO_4 1.0. The pH was adjusted to 7.35 when bubbled with 95% O_2/5% CO_2 using 1 M KOH (Fluka Analytical, Sigma-Aldrich). After cutting, the slices were incubated for >1 h at 30°C in incubating solution containing (mM): NaCl 126.0, KCl 2.5, $CaCl_2 \cdot 2H_2O$ 2.0, $MgCl_2 \cdot 6H_2O$ 2.0, $NaHCO_3$ 26.0, glucose 10.0, pH 7.4 when bubbled with 95% O_2/5% CO_2 (all reagents for solutions were purchased from Sigma-Aldrich).

Electrophysiology

Whole cell patch clamp was performed on MNs from the lumbar segments using 2–4 MΩ glass electrodes pulled from glass capillary tubes (Item #TW150F-4, World Precision Instruments, Sarasota, FL, USA) with a Flaming-Brown P-97 (Sutter Instrument Company, Novato, CA, USA). Electrodes were positioned using

a Sutter Instrument MP-285 motorized micromanipulator (Sutter Instrument Company). Whole-cell patch clamp measurements were performed at room temperature using the Multiclamp700B amplifier (Molecular Devices, Burlingame, CA, USA) and Winfluor software (University of Strathclyde, Glasgow, Scotland). Briefly, slices were perfused with a modified Ringer's solution containing (in mM): 111 NaCl, 3.09 KCl, 25.0 $NaHCO_3$, 1.10 KH_2PO_4, 1.26 $MgSO_4$, 2.52 $CaCl_2$, and 11.1 glucose. The solution was oxygenated with 95% O_2/5% CO_2 and the perfusion rate was 2.5 – 3.0 ml/min. Patch electrodes contained (in mM) 138 K-gluconate, 10 HEPES, 5 ATP-Mg, 0.3 GTP-Li and Texas Red dextran (150 µM, 3000 MW, from Invitrogen, Life Technologies, Grand Island, NY, USA). In voltage-clamp mode, fast and slow capacitance transients, as well as whole-cell capacitance, were compensated using the automatic capacitance compensation on the Multiclamp. Holding potential was set at −90 mV, and neurons were subjected to slow, depolarizing voltage ramps of 22.5 mV s^{-1}, bringing the cell to 0 mV in 4 s, and then back to the holding potential in the following 4 s. In current clamp, neurons were subjected to depolarizing current ramps for testing I-on (the current level at firing onset), I-off (the current level at cessation of firing), and the slope of the frequency–current relationship. Negative current was often necessary to prevent action potential (AP) firing.

Neuron Selection

Glycinergic interneurons were visually selected for recording based on 1) expression of GFP, and 2) location near the MN pools. Neurons that did not repetitively fire or did not maintain a resting membrane potential below -35 mV were excluded from electrophysiological analysis. Neurons that were not clearly stained with Texas Red after patch clamp and/or could not be imaged clearly were not included in anatomical analysis.

Electrophysiological analysis

Persistent inward current (PIC) parameters were measured after subtraction of leak current. Onset was defined as the voltage at which the current began to deviate from the horizontal, leak-subtracted trace. PIC peak was the voltage at which the PIC reached peak amplitude. The linear portion of leak current (usually between -90 and -75 mV) was used to calculate whole cell input resistance. The first action potential in the train evoked by a depolarizing current ramp in current clamp mode was used to measure all parameters relating to action potentials. Threshold voltage was defined as the voltage at which the slope exceeded 10 V/s. Threshold for action potential firing was tested in two ways. The first was to use the voltage at firing onset from the current ramps up to 130 pA/s (in current clamp). The second was the voltage at which a single action potential could be evoked with a current step. Action potential overshoot

is the voltage past 0 mV the first spike reaches. Duration of the action potential is measured at half of action potential height (height is defined as overshoot – threshold voltage). Rates of rise and fall are defined as the peak and the trough of the first derivative of the action potential profile.

Immunohistochemistry

Immediately after electrophysiological recording, slices were fixed in (4%) paraformaldehyde for 24 h. As described by Kupferschmidt and colleagues (Kupferschmidt et al., 2015), sections were then incubated in sodium borohydride ($NaBH_4$; 5mg/mL in diH_2O) to quench aldehyde-induced catecholamine fluorescence and reduce free aldehyde groups, followed by Sudan Black B solution (0.2% in 70% ethanol). Slices were washed twice for 30 min in room temperature PBS to extinguish the immunohistochemistry reaction. Slices were blocked using 2% normal horse serum in PBST (0.2% Triton-X100 in PBS) for 4 h, and incubated in PBST with rabbit anti-Texas Red antibody (polyclonal IgG, 1:2000, ThermoFisher Scientific®, A-6399); mouse anti-Calbindin-D-28K (monoclonal; 1:3000, Sigma, C9848) for 72 h at 4°C. Following four washes in PBST over a total of 16–24 h, slices were incubated in the appropriate fluorescent dye-conjugated secondary antibodies (goat anti-rabbit IgG, Texas Red-conjugated, and goat anti-mouse IgG, Cyanine5-conjugated, both ThermoFisher Scientific®, 1:500, T-6391, and 1:500, A10524, respectively) for 48 h. Then they were washed again in 0.1M PBS and DAPI treated for 5 min, washed and covered using Fluoromount® and glass coverslips.

Morphological analysis

Neuron morphology was assessed from two types of images: 1) 2 photon image stacks of live neurons taken immediately after obtaining electrophysiological parameters, and 2) confocal image stacks taken after fixation and tissue processing. Images collected using these two methods were analyzed separately. Measurements from 2-photon images included measurements from both soma and dendrites (soma volume, maximum soma cross-sectional area, soma perimeter in the largest plane, soma surface area, number of primary dendrites, and average dendrite length, dendrite surface area and dendrite volume). Measurements from confocal images only included soma measurements.

Two photon imaging: An Olympus BX-51WIF microscope fitted with an Olympus 40x/0.8NA water-dipping objective lens was used. Two-photon excitation fluorescence microscopy was performed with a galvanometer-based Coherent Chameleon Ultra II laser (Coherent, Santa Clara, CA, USA) tuned to 900 nm. A red Bio-Rad 2100MPD photomultiplier tube (Bio-Rad, Hercules, CA, USA) (570 – 650 nm) was used to collect emission in the red channel. Z-stacks were obtained for each interneuron at 1024 x 1024 pixels (308 x 308 µm) resolution and roughly 100 µm in depth (step size 1 µm). From these Z-stacks, Texas

Red® -filled neurons were three-dimensionally reconstructed using Neurolucida software (MBF Bioscience, Williston, VT, USA).

Confocal imaging: Sections were observed with a confocal laser microscope (LSM510, Zeiss, Oberkochen, Darmstadt, Germany) with argon (488 nm) and helium-neon (543 nm) lasers and a 20X objective. Each confocal image obtained in triple staining experiments was split into three channels. Co-localization analysis of CBD, Texas Red and GlyT2 positive cells included visual inspection of labeling, size, and shape of the cell through the stack. From these Z-stacks, GlyT2 positive interneurons were three-dimensionally reconstructed using Neurolucida software (MBF Bioscience, Williston, VT, USA). CBD positive cells were counted using ImageJ (National Institutes of Health, Bethesda, MD).

Statistical analysis

The assumptions of homogeneity of variances and the normality of the distribution of values for each measured characteristic were evaluated with Levene's and Shapiro-Wilk tests, respectively. Group comparisons (WT vs SOD1) were performed using ANOVA on characteristics that satisfied both conditions and using the Kruskal-Wallis test for the rest of the characteristics. Results are presented as means ± SEM. Significance level was set at $p \leq 0.05$.

Statistical modeling: Random Forest and Principal Component Analysis

As it was not possible to confirm or rule out RC identity in the majority of our neurons using immunohistochemistry, we created statistical models based on those we had tested to predict RC identity among remaining untested neurons. To do this, we employed a random forest method of statistical learning that generates a large number of decision trees, each constructed using a different, randomly selected (with replacement) subset of the training data set. Thus, all variables in the dataset were first split into 8 subgroups of related variables. Groups included membrane properties, action potential measurements, PIC properties, firing frequency measurements, AHP parameters, I_H characteristics, soma measurements and dendritic properties. For example, all variables pertaining to PIC characteristics (PIC onset, peak voltage, PIC amplitude and normalized amplitude) were grouped. Next, a random forest model (Breiman, 2001) was created for each subgroup of variables varying the number of measurements to include in each tree. This method determined the number of variables that yielded the most accurate model. The reason this was performed (instead of including all measured parameters) is that models with larger numbers of variables tend to overfit the training dataset and fail to classify accurately unseen/test cases. Therefore, it was essential to distill down our parameters to only include the most important variables for classifying neurons as RC or non-RC. The decision trees are

445 then used to classify an observation by selecting the most common label among multiple trees. Random
446 forest allows varying two parameters: the number of variables to consider when building each tree and
447 the number of generated trees. One can choose a set of these two parameters that yields the most
448 optimal model. The random forest model with the lowest error was then used to evaluate the most
449 important variables in each subgroup for distinguishing between RCs and non-RCs. Here we used Mean
450 Decrease in Accuracy Index to evaluate the importance of the various measured characteristics of the
451 neurons in predicting RCs vs non-RCs. After the important variables in each subgroup were identified, a
452 dataset was created with only these variables and the above process was repeated using these
453 important variables. Model accuracy was evaluated by using a leave-one-out cross validation (LOOCV).
454 The accuracy for the best random forest model created from the previously determined important
455 variables was 79%. The best random forest model was then used to predict the RC/non-RC classification
456 for untested cells in the dataset. Once the RC/non-RC classification was determined, normality and
457 homogeneity tests were run on each group followed by ANOVA and Kruskal Wallis in order to determine
458 group differences between WT RCs and SOD1 RCs as well as between WT non-RCs and SOD1 non-RCs.
459 Principal components analysis (PCA) (Hotelling, 1933) of each previously created subgroup of variables
460 was also evaluated for predictive value. The scores from the first two principal components in each
461 subgroup were used in a logistic regression model to predict the known CBD-tested cells. Using PCA, the
462 most important variables were identified as the same as those identified by the random forest method.
463 The model accuracy was also tested using LOOCV. The best PCA model accuracy was 70%, therefore,
464 the random forest model (with 79% accuracy based on LOOCV) was selected to predict classification of
465 the remaining untested neurons rather than this method.
466

467 **Acknowledgments**

468 This project was funded by a springboard fellowship from Target ALS to KAQ and a University of Rhode
469 Island Graduate School Tuition Scholarship to LMM. The authors thank Drs Emily Reedich and Claudia
470 Fallini for comments on the initial draft of the manuscript.
471

References

Akay T (2014) Long-term measurement of muscle denervation and locomotor behavior in individual wild-type and ALS model mice. J Neurophysiol 111:694–703.

Allodi I, Montañana-Rosell R, Selvan R, Löw P, Kiehn O (2020) Locomotor deficits in ALS mice are paralleled by loss of V1-interneuron-connections onto fast motor neurons. bioRxiv:2020.06.23.166389 Available at: http://biorxiv.org/content/early/2020/06/23/2020.06.23.166389.abstract.

Amendola J, Durand J (2008) Morphological differences between wild-type and transgenic superoxide dismutase 1 lumbar motoneurons in postnatal mice. J Comp Neurol 511:329–341.

Andreadou E, Kapaki E, Kokotis P, Paraskevas GP, Katsaros N, Libitaki G, Petropoulou O, Zis V, Sfagos C, Vassilopoulos D (2008) Plasma glutamate and glycine levels in patients with amyotrophic lateral sclerosis. In Vivo (Brooklyn) 22:137–142.

Avossa D, Grandolfo M, Mazzarol F, Zatta M, Ballerini L (2006) Early signs of motoneuron vulnerability in a disease model system: Characterization of transverse slice cultures of spinal cord isolated from embryonic ALS mice. Neuroscience 138:1179–1194.

Bae JS, Simon NG, Menon P, Vucic S, Kiernan C, Doyle AC, Case-book T, Holmes S (2013) The Puzzling Case of Hyperexcitability in Amyotrophic Lateral Sclerosis What Really is Hyperexcitability in ALS ? How Can We Objectively Assess. J Clin Neurol 9:65–74.

Bensimon G, Lacomblez L, Meininger V (1994) A Controlled Trial of Riluzole in Amyotrophic Lateral Sclerosis. N Engl J Med 330:585–591.

Branchereau P, Martin E, Supiot L, Hodeib F, Laupénie A, Dalvi U, Zhu H, Cazenave W, Cattaert D (2019) Relaxation of synaptic inhibitory events as a compensatory mechanism in fetal SOD spinal motor networks. Elife 8:1–28.

Breiman L (2001) Random forests. Mach Learn 45:5–32.

Casas C, Herrando-Grabulosa M, Manzano R, Mancuso R, Osta R, Navarro X (2013) Early presymptomatic cholinergic dysfunction in a murine model of amyotrophic lateral sclerosis. Brain Behav 3:145–158.

Chang Q, Martin LJ (2009a) Glycinergic Innervation of Motoneurons Is Deficient in Amyotrophic Lateral Sclerosis Mice A Quantitative Confocal Analysis. Am J Pathol 174:574–585.

Chang Q, Martin LJ (2009b) Glycinergic innervation of motoneurons is deficient in amyotrophic lateral sclerosis mice: A quantitative confocal analysis. Am J Pathol 174:574–585.

Clark RM, Blizzard CA, Young KM, King AE, Dickson TC (2017) Calretinin and Neuropeptide y interneurons are differentially altered in the motor cortex of the SOD1 G93A mouse model of ALS. Sci Rep 7:1–13

503 Available at: http://dx.doi.org/10.1038/srep44461.
504 Clark RM, Brizuela M, Blizzard CA, Dickson TC (2018) Reduced excitability and increased neurite
505 complexity of cortical interneurons in a familial mouse model of amyotrophic lateral sclerosis. Front Cell
506 Neurosci 12:1–7.
507 Delestrée N, Manuel M, Iglesias C, Elbasiouny SM, Heckman CJ, Zytnicki D (2014) Adult spinal
508 motoneurones are not hyperexcitable in a mouse model of inherited amyotrophic lateral sclerosis. J
509 Physiol 592:1687–1703.
510 Devlin AC, Burr K, Borooah S, Foster JD, Cleary EM, Geti I, Vallier L, Shaw CE, Chandran S, Miles GB
511 (2015) Human iPSC-derived motoneurons harbouring TARDBP or C9ORF72 ALS mutations are
512 dysfunctional despite maintaining viability. Nat Commun 6:1–12 Available at:
513 http://dx.doi.org/10.1038/ncomms6999.
514 Dukkipati SS, Chihi A, Wang Y, Elbasiouny SM (2016) Experimental Design and Data Analysis Issues
515 Contribute to Inconsistent Results of C-Bouton Changes in Amyotrophic Lateral Sclerosis. eNeuro 4:1–
516 13.
517 Dukkipati SS, Garrett TL, Elbasiouny SM (2018) The vulnerability of spinal motoneurons and soma size
518 plasticity in a mouse model of amyotrophic lateral sclerosis. J Physiol 596:1723–1745.
519 Filipchuk AA, Durand J (2012) Postnatal dendritic development in lumbar motoneurons in mutant
520 superoxide dismutase 1 mouse model of amyotrophic lateral sclerosis. Neuroscience 209:144–154
521 Available at: http://dx.doi.org/10.1016/j.neuroscience.2012.01.046.
522 Genç B, Jara JH, Lagrimas AKB, Pytel P, Roos RP, Mesulam MM, Geula C, Bigio EH, Özdinler PH (2017)
523 Apical dendrite degeneration, a novel cellular pathology for Betz cells in ALS. Sci Rep 7:1–10 Available at:
524 http://dx.doi.org/10.1038/srep41765.
525 Gunes ZI, Kan VWY, Ye XQ, Liebscher S (2020) Exciting Complexity: The Role of Motor Circuit Elements in
526 ALS Pathophysiology. Front Neurosci 14:1–30.
527 Hayashi H, Suga M, Satake M, Tsubaki T (1981) Reduced glycine receptor in the spinal cord in
528 amyotrophic lateral sclerosis. Ann Neurol 9:292–294.
529 Hegedus J, Putman CT, Gordon T (2007) Time course of preferential motor unit loss in the SOD1G93A
530 mouse model of amyotrophic lateral sclerosis. Neurobiol Dis 28:154–164.
531 Herron LR, Miles GB (2012) GENDER-SPECIFIC PERTURBATIONS IN MODULATORY INPUTS TO
532 MOTONEURONS IN A MOUSE MODEL OF AMYOTROPHIC LATERAL SCLEROSIS. Neuroscience 226:313–
533 323 Available at: http://dx.doi.org/10.1016/j.neuroscience.2012.09.031.

534 Hossaini M, Cano SC, Van Dis V, Haasdijk ED, Hoogenraad CC, Holstege JC, Jaarsma D (2011) Spinal
535 inhibitory interneuron pathology follows motor neuron degeneration independent of glial mutant
536 superoxide dismutase 1 expression in SOD1-ALS mice. J Neuropathol Exp Neurol 70:662–677.
537 Hotelling H (1933) Analysis of a complex of statistical variables into Principal Components. J Educ
538 Psychol 24:417–441.
539 Howells J, Sangari S, Matamala JM, Kiernan MC, Marchand-Pauvert V, Burke D (2020) Interrogating
540 interneurone function using threshold tracking of the H reflex in healthy subjects and patients with
541 motor neurone disease. Clin Neurophysiol.
542 Irvin CW, Kim RB, Mitchell CS (2015) Seeking homeostasis: Temporal trends in respiration, oxidation, and
543 calcium in SOD1 G93A amyotrophic lateral sclerosis mice. Front Cell Neurosci 9:1–11.
544 Jensen DB, Kadlecova M, Allodi I, Meehan CF (2020) Spinal motoneurones are intrinsically more
545 responsive in the adult G93A SOD1 mouse model of Amyotrophic Lateral Sclerosis. J Physiol.
546 Kim J, Hughes EG, Shetty AS, Arlotta P, Goff LA, Bergles DE, Brown SP (2017) Changes in the Excitability
547 of Neocortical Neurons in a Mouse Model of Amyotrophic Lateral Sclerosis Are Not Specific to
548 Corticospinal Neurons and Are Modulated by Advancing Disease. J Neurosci 37:9037–9053 Available at:
549 http://www.jneurosci.org/lookup/doi/10.1523/JNEUROSCI.0811-17.2017.
550 Kuo JJ, Schonewille M, Siddique T, Schults AN, Fu R, Bar PR, Anelli R, Heckman C, Kroese AB (2004)
551 Hyperexcitability of Cultured Spinal Motoneurons From Presymptomatic ALS Mice. J Neurophysiol
552 91:571–575 Available at: http://jn.physiology.org/cgi/doi/10.1152/jn.00665.2003.
553 Kuo JJ, Siddique T, Fu R, Heckman CJ (2005) Increased persistent Na+ current and its effect on
554 excitability in motoneurones cultured from mutant SOD1 mice. J Physiol 563:843–854.
555 Kuo SW, Binder MD, Heckman CJ (2020) Excessive Homeostatic Gain in Spinal Motoneurons in a Mouse
556 Model of Amyotrophic Lateral Sclerosis. Sci Rep 10.
557 Kupferschmidt DA, Cody PA, Lovinger DM, Davis MI (2015) Brain BLAQ: Post-hoc thick-section
558 histochemistry for localizing optogenetic constructs in neurons and their distal terminals. Front
559 Neuroanat 9:1–9.
560 Landoni LM, Myles JR, Wells TL, Mayer WP, Akay T (2019) Cholinergic modulation of motor neurons
561 through the C-boutons are necessary for the locomotor compensation for severe motor neuron loss
562 during amyotrophic lateral sclerosis disease progression. Behav Brain Res 369.
563 Leroy F, Lamotte d'Incamps B, Imhoff-Manuel RD, Zytnicki D (2014) Early intrinsic hyperexcitability does
564 not contribute to motoneuron degeneration in amyotrophic lateral sclerosis. Elife 3:1–25.

565 Malessa S, Leigh PN, Bertel O, Sluga E, Hornykiewicz O (1991) Amyotrophic lateral sclerosis: glutamate
566 dehydrogenase and transmitter amino acids in the spinal cord. J Neurol Neurosurg Psychiatry 54:984–
567 988.
568 Martin E, Cazenave W, Cattaert D, Branchereau P (2013) Embryonic alteration of motoneuronal
569 morphology induces hyperexcitability in the mouse model of amyotrophic lateral sclerosis. Neurobiol Dis
570 54:116–126.
571 Martin LJ, Liu Z, Chen K, Price AC, Pan Y, Swaby JA, Golden WC (2007) Motor Neuron Degeneration in
572 Amyotrophic Lateral Sclerosis Mutant Superoxide Dismutase-1 Transgenic Mice: Mechanisms of
573 Mitochondriopathy and Cell Death. J Comp Neurol 500:20–46.
574 Martinez-Silva M de L, Imhoff-Manuel RD, Sharma A, Heckman C, Shneider NA, Roselli F, Zytnicki D,
575 Manuel M (2018) Hypoexcitability precedes denervation in the large fast-contracting motor units in two
576 unrelated mouse models of ALS. Elife 7:1–26.
577 McGown A, McDearmid JR, Panagiotaki N, Tong H, Al Mashhadi S, Redhead N, Lyon AN, Beattie CE, Shaw
578 PJ, Ramesh TM (2013) Early interneuron dysfunction in ALS: Insights from a mutant sod1 zebrafish
579 model. Ann Neurol 73:246–258.
580 Medelin M, Rancic V, Cellot G, Laishram J, Veeraraghavan P, Rossi C, Muzio L, Sivilotti L, Ballerini L (2016)
581 Altered development in GABA co-release shapes glycinergic synaptic currents in cultured spinal slices of
582 the SOD1G93Amouse model of amyotrophic lateral sclerosis. J Physiol 594:3827–3840.
583 Milan L, Courtand G, Cardoit L, Masmejean F, Barrière G, Cazalets JR, Garret M, Bertrand SS (2015) Age-
584 related changes in pre- and postsynaptic partners of the cholinergic C-boutons in wild-type and
585 SOD1G93Alumbar motoneurons. PLoS One 10:1–21.
586 Niebroj-Dobosz I, Janik P (1999) Amino acids acting as transmitters in amyotrophic lateral sclerosis (ALS).
587 Acta Neurol Scand 100:6–11.
588 Ozdinler PH, Benn S, Yamamoto TH, Guzel M, Brown RH, Macklis JD (2011) Corticospinal Motor Neurons
589 and Related Subcerebral Projection Neurons Undergo Early and Specific Neurodegeneration in
590 hSOD1G93A Transgenic ALS Mice. J Neurosci 31:4166–4177 Available at:
591 http://www.jneurosci.org/cgi/doi/10.1523/JNEUROSCI.4184-10.2011.
592 Pambo-Pambo A, Durand J, Gueritaud J-P (2009) Early excitability changes in lumbar motoneurons of
593 transgenic SOD1G85R and SOD1G(93A-Low) mice. J Neurophysiol 102:3627–3642 Available at:
594 http://www.ncbi.nlm.nih.gov/pubmed/19828728.
595 Pieri M, Carunchio I, Curcio L, Mercuri NB, Zona C (2009) Increased persistent sodium current

596 determines cortical hyperexcitability in a genetic model of amyotrophic lateral sclerosis. Exp Neurol
597 215:368–379 Available at: http://dx.doi.org/10.1016/j.expneurol.2008.11.002.
598 Piotrkiewicz M, Hausmanowa-Petrusewicz I (2011) Motoneuron afterhyperpolarisation duration in
599 amyotrophic lateral sclerosis. J Physiol 589:2745–2754.
600 Plaitakis A, Constantakakis E (1993) Altered metabolism of excitatory amino acids, N-acetyl-aspartate
601 and N-acetyl-aspartylglutamate in amyotrophic lateral sclerosis. Brain Res Bull 30:381–386.
602 Pullen AH, Athanasiou D (2009) Increase in presynaptic territory of C-terminals on lumbar motoneurons
603 of G93A SOD1 mice during disease progression. Eur J Neurosci 29:551–561.
604 Pun S, Santos AF, Saxena S, Xu L, Caroni P (2006) Selective vulnerability and pruning of phasic
605 motoneuron axons in motoneuron disease alleviated by CNTF. Nat Neurosci 9:408–419.
606 Quinlan KA, Kajtaz E, Ciolino JD, Imhoff-Manuel RD, Tresch MC, Heckman CJ, Tysseling VM (2017)
607 Chronic electromyograms in treadmill running SOD1 mice reveal early changes in muscle activation. J
608 Physiol 595:5387–5400.
609 Quinlan KA, Lamano JB, Samuels J, Heckman CJ (2015) Comparison of dendritic calcium transients in
610 juvenile wild type and SOD1G93A mouse lumbar motoneurons. Front Cell Neurosci 9:1–13 Available at:
611 http://journal.frontiersin.org/article/10.3389/fncel.2015.00139/abstract.
612 Quinlan KA, Schuster JE, Fu R, Siddique T, Heckman CJ (2011) Altered postnatal maturation of electrical
613 properties in spinal motoneurons in a mouse model of amyotrophic lateral sclerosis. J Physiol 589:2245–
614 2260 Available at: http://doi.wiley.com/10.1113/jphysiol.2010.200659.
615 Raynor EM, Shefner JM (1994) Recurrent inhibition is decreased in patients with amyotrophic lateral
616 sclerosis. Neurology 44:2148–2153.
617 Rothstein JD, Martin LJ, Kuncl RW (1992) Decreased Glutamate Transport by the Brain and Spinal Cord in
618 Amyotrophic Lateral Sclerosis. N Engl J Med 326:1464–1468.
619 Saba L, Viscomi MT, Caioli S, Pignataro A, Bisicchia E, Pieri M, Molinari M, Ammassari-Teule M, Zona C
620 (2016) Altered Functionality, Morphology, and Vesicular Glutamate Transporter Expression of Cortical
621 Motor Neurons from a Presymptomatic Mouse Model of Amyotrophic Lateral Sclerosis. Cereb Cortex
622 26:1512–1528.
623 Saba L, Viscomi MT, Martini A, Caioli S, Mercuri NB, Guatteo E, Zona C (2019) Modified age-dependent
624 expression of NaV1.6 in an ALS model correlates with motor cortex excitability alterations. Neurobiol Dis
625 130:104532 Available at: https://doi.org/10.1016/j.nbd.2019.104532.
626 Sangari S, Iglesias C, El Mendili MM, Benali H, Pradat PF, Marchand-Pauvert V (2016) Impairment of

627 sensory-motor integration at spinal level in amyotrophic lateral sclerosis. Clin Neurophysiol 127:1968–
628 1977.
629 Saxena S, Roselli F, Singh K, Leptien K, Julien JP, Gros-Louis F, Caroni P (2013) Neuroprotection through
630 Excitability and mTOR Required in ALS Motoneurons to Delay Disease and Extend Survival. Neuron
631 80:80–96 Available at: http://dx.doi.org/10.1016/j.neuron.2013.07.027.
632 Shefner JM, Logigian EL (1998) The mixed nerve silent period in normal subjects and patients with
633 amyotrophic lateral sclerosis. Electromyogr Clin Neurophysiol 38:505–510.
634 Vinsant S, Mansfield C, Jimenez-Moreno R, Moore VDG, Yoshikawa M, Hampton TG, Prevette D, Caress
635 J, Oppenheim RW, Milligan C (2013a) Characterization of early pathogenesis in the SOD1G93A mouse
636 model of ALS: Part II, results and discussion. Brain Behav 3:431–457.
637 Vinsant S, Mansfield C, Jimenez-Moreno R, Moore VDG, Yoshikawa M, Hampton TG, Prevette D, Caress
638 J, Oppenheim RW, Milligan C (2013b) Characterization of early pathogenesis in the SOD1G93A mouse
639 model of ALS: Part I, background and methods. Brain Behav 3:335–350.
640 Wainger BJ, Kiskinis E, Mellin C, Wiskow O, Han SSW, Sandoe J, Perez NP, Williams LA, Lee S, Boulting G,
641 Berry JD, Brown RH, Cudkowicz ME, Bean BP, Eggan K, Woolf CJ (2014) Intrinsic membrane
642 hyperexcitability of amyotrophic lateral sclerosis patient-derived motor neurons. Cell Rep 7:1–11
643 Available at: http://dx.doi.org/10.1016/j.celrep.2014.03.019.
644 Whitehouse PJ, Wamsley JK, Zarbin MA, Price DL, Tourtellotte WW, Kuhar MJ (1983) Amyotrophic
645 lateral sclerosis: Alterations in neurotransmitter receptors. Ann Neurol 14:8–16.
646 Wootz H, Fitzsimons-Kantamneni E, Larhammar M, Rotterman TM, Enjin A, Patra K, André E, Van
647 Zundert B, Kullander K, Alvarez FJ (2013) Alterations in the motor neuron-renshaw cell circuit in the
648 Sod1G93Amouse model. J Comp Neurol 521:1449–1469.
649 Zeilhofer HU, Studler B, Arabadzisz D, Schweizer C, Ahmadi S, Layh B, Bösl MR, Fritschy JM (2005)
650 Glycinergic neurons expressing enhanced green fluorescent protein in bacterial artificial chromosome
651 transgenic mice. J Comp Neurol 482:123–141.
652
653